PREDICTION APPROACH OF RISE PART OF REAL-TIME SEISMIC INTENSITY

Hisahiko KUBO[1] and Takashi KUNUGI[2]

[1] Member, Dr. Sc., Chief Researcher, Network Center for Earthquake, Tsunami and Volcano,
National Research Institute for Earth Science and Disaster Resilience, Tsukuba, Japan,
hkubo@bosai.go.jp
[2] Member, Dr. Sc., Head, Strong Motion Seismograph Network Laboratory,
Network Center for Earthquake, Tsunami and Volcano,
National Research Institute for Earth Science and Disaster Resilience, Tsukuba, Japan,
kunugi@bosai.go.jp

ABSTRACT: In this study, we proposed a method to simply predict the rise part of real-time seismic intensity time-series. First, the duration between the P-wave arrival and achieving 95% of the maximum value of real-time seismic intensity was taken to be the characteristic time of the rise part. Then, its prediction equation using hypocentral distance, moment magnitude, source depth, average S-wave velocity up to 30 m depth, and top depth to the layer whose S-wave velocity is 1,400 m/s as explanatory variables was developed by regression analysis based on strong-motion records of 41 earthquakes. In addition, an approximate function based on a logarithmic function was proposed to reproduce the time-series shape of the rise part. Combining the prediction equation and function, the rise part of real-time seismic intensity at any point could be predicted and reproduced. We verified the effectiveness and limitations of this prediction approach with records of the 2016 Kumamoto earthquake and the 2011 Tohoku earthquake.

Keywords: *Real-time seismic intensity, Rise part, Time-series analysis, Prediction equation*

1. INTRODUCTION

Seismic intensity is a commonly-used ground motion indicator in the field of earthquake disaster reduction in Japan. The seismic intensity published by the Japan Meteorological Agency (JMA)[1] is calculated from the digital seismic waveform records and is a static index that is derived from waveform records with a certain time length. Kunugi et al.[2] proposed a method for calculating seismic intensity in real-time using recursive filters in the time domain; the method exhibited both high calculation accuracy

and speed. The "real-time seismic intensity" calculated by this method can be considered a dynamic seismic motion index. The online service "Kyoshin Monitor" provided by the National Research Institute for Earth Science and Disaster Resilience (NIED) displays the distribution of real-time seismic intensity every second across Japan. When an earthquake occurs, it presents the propagation of the earthquake shaking through color change.

A ground motion prediction equation that predicts seismic intensity has been proposed[3, 4]. Nojima et al.[5]–[7] have worked on predicting the duration of seismic intensity. However, no studies have been conducted on the evaluation of the temporal characteristics of real-time seismic intensity and the prediction of its time-series. In this study, we propose a simple method to predict and reproduce the time-series of real-time seismic intensity, focusing on the rise part between the onset of shaking and maximum shaking. Combining this prediction method with the existing ground motion prediction equation for seismic intensity enables the simple prediction of a real-time seismic intensity time-series for any earthquake at any location. This can be used to provide highly realistic information on the time-series of ground motion in the pre-training of earthquake disasters based on earthquake scenarios.

Figure 1 shows examples of real-time seismic intensity observations. Figure 1(a) shows the observations at NIG022 for the 2004 Niigata Chuetsu earthquake (Event #12, M_w 6.6 in Table A1); Figure 1(b) shows the observations at GNM009 for this event; Figure 1(c) shows the observations at NIG022 for Event #14 (aftershock of Event #12). The real-time seismic intensities increased as the P-wave arrived and reached a maximum after the arrival of S-wave. As shown in Figs. 1(a) and 1(b), the record at the station with a large hypocentral distance (GNM009, 105.8 km) had a longer rise time from the P-wave arrival to its peak compared to that at the station having a small hypocentral distance (NIG022, 28.6 km). This can be mainly attributed to the fact that the difference in travel time between the P- and S-waves increases with respect to the distance. Moreover, the time from the S-wave arrival to its peak also increases as the hypocentral distance increases. As shown in Figs. 1(a) and 1(c), the rise time differs depending on the earthquake magnitude, even for the same observation stations and almost identical hypocentral distances; a larger earthquake magnitude results in a longer rise time. Thus, the rise time for real-time seismic intensity varies depending on the hypocentral distance and earthquake magnitude. This is probably because the difference in travel time between the P- and S-waves, the relative predominance between the direct and subsequent waves, and the time difference between the rupture initiation and the peak of seismic wave radiation depend on the hypocentral distance and earthquake magnitude. This indicates that the rise time could be predicted by a regression equation using the hypocentral distance and the earthquake magnitude as the explanatory variables. The shape of the rise part of real-time seismic intensity is complex (Fig. 1) because the rise part of real-time seismic intensity is formed by overlapping not only P- and S-waves of body waves, but also the subsequent waves and surface waves. The full reproduction of this shape requires the complete modeling of each seismic wave and may incur a high computational cost. As the aim of this study is simple prediction, we considered the time-series of the rise part as a single function and proposed a function that approximates its shape.

In this study, we developed a prediction equation for the rise time of real-time seismic intensity using regression analysis based on past records and devised an approximation function that simulates the time-series shape of the rise part. The proposed method was then applied to the records of the 2016 Kumamoto earthquake and the 2011 Tohoku earthquake to evaluate its prediction performance.

Elapsed Time from T_P (s)

(a) Event #12 (M_w 6.6), NIG022, X 28.6 km, D_{MAX95} 7.0 s, I_r^{MAX} 5.1

(b) Event #12 (M_w 6.6), GNM009, X 105.8 km, D_{MAX95} 16.9 s, I_r^{MAX} 3.8

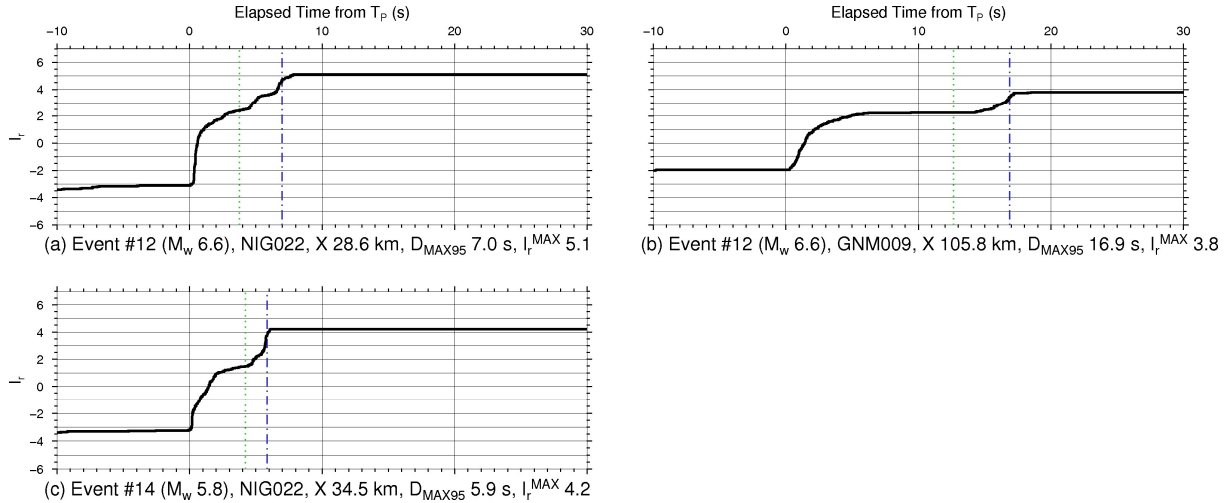(c) Event #14 (M_w 5.8), NIG022, X 34.5 km, D_{MAX95} 5.9 s, I_r^{MAX} 4.2

Fig. 1   Observation examples of real-time seismic intensity (a) at NIG022 for Event #12 (Table A1), (b) at GNM009 for Event #12, and (c) at NIG022 for Event #14. 0 s on the horizontal axis corresponds to the theoretical P-wave travel time. The green dotted line indicates S-wave arrival time, and the blue dash-dot line indicates T_{MAX95}.

2. PREDICTION OF RISE TIME

The duration of ground motion has been previously investigated[8]–[10], and the duration of seismic intensity and Arias intensity[11] have also been studied[5]–[7], [12]–[14]. These studies focused on the net time beyond a certain absolute or relative value, or the time from the first rise to the last fall. To predict the shapes of the time-series of real-time seismic intensity, it is necessary to predict the time difference between the start time and the time of maximum value attainment. Because no previous study has focused on this, we developed a novel prediction equation for the rise time of real-time seismic intensity.

To prepare the dataset, a time-series of real-time seismic intensity with a sampling of 0.01 s was calculated based on Kunugi et al.[2] and the NIED[15], [16]. First, three components of the original acceleration records (two horizontal components and one vertical component) were filtered by a time domain approximation filter. Thereafter, the vector sum of the filtered waveforms was converted to the time-series of values equivalent to seismic intensity. Then, the time-series of real-time seismic intensity was obtained through a judgment process that sets the value with a total duration of 0.3 s as the real-time seismic intensity in that time interval. This judgment process was conducted from the beginning of the record in increments of 0.01 s. The reference range in this judgment process was the time-series information between the target time and 60 s before. For the convenience of the duration judgment process, the discretization in intervals of 0.001 was conducted by setting the lower and upper limits of the value in the conversion to the measured seismic intensity equivalent values, corresponding to −6.0 and 8.0, respectively. Therefore, the calculated values of real-time seismic intensity range from −6.0 to 8.0, and the value at the beginning of the record was always −6.0.

We prepared the real-time seismic intensities using the above processing for 8,022 records observed by K-NET and KiK-net of NIED[17], [18] for the 41 events summarized in Table A1. In the selection process of the records, first, we referred to the JMA seismic intensity database[19] to find earthquakes that recorded a maximum seismic intensity of 6 lower or more in the period from 1996 to 2020. Thereafter, we selected the records for these events that satisfied any of the following conditions: (1) real-time seismic intensity was greater than −6.0 at the arrival of P-wave; (2) real-time seismic intensity was equal

to or less than 0.0 at the arrival of P-wave; (3) maximum value of real-time seismic intensity was equal to or more than 2.0; (4) and records started 5 s before the arrival of P-wave. Finally, we selected the records of only the 41 events in Table A1 that were available at ten or more observation stations, including stations near the epicenter. In this final step, the 2011 Tohoku earthquake and the 2016 Kumamoto earthquake were excluded from these events because the former was a massive earthquake and the latter triggered aftershocks immediately after the main shock.

I_r^{MAX95} is defined as 95% of the relative difference between the maximum value of real-time seismic intensity, I_r^{MAX}, and the threshold value, I_r^0, and is calculated as:

$$I_r^{MAX95} = 0.95 \times (I_r^{MAX} - I_r^0) + I_r^0 \tag{1}$$

where I_r^0 corresponds to non-earthquake real-time seismic intensity. Figure 2 shows a histogram of the real-time seismic intensity 2 s before the arrival of P-wave. The value of the non-earthquake real-time seismic intensity varies depending on the installation environment of seismograph and the time of day, but is often between −4.5 and −2.5. Therefore, an overall average of −3.5 was adopted as I_r^0. The time when the real-time seismic intensity value reached I_r^{MAX95} was defined as T_{MAX95}, and the difference between the P-wave arrival time, T_p, and T_{MAX95} was defined as D_{MAX95}:

$$D_{MAX95} = T_{MAX95} - T_p \tag{2}$$

The theoretical travel time information of the P-wave was used as T_p. JMA2001[20] was used for the velocity structure to calculate the theoretical travel time. D_{MAX95} and T_{MAX95} for the observation examples are shown in Fig. 1. The tendency of the rise time for real-time seismic intensity becoming longer as the hypocentral distance or earthquake magnitude became larger, as discussed in Section 1, reflects in the values of D_{MAX95} in Fig. 1. Therefore, we considered D_{MAX95} to be a characteristic time of the rise part of real-time seismic intensity, and we empirically developed its prediction equation from past records. Considering previous studies for seismic intensity and its duration[3]–[7], we considered that D_{MAX95} was related to hypocentral distance, earthquake magnitude, source depth, and underground structures just below the observation point. Therefore, we characterized D_{MAX95} with the hypocentral distance X (km), moment magnitude M_w, source depth H (km), average S-wave velocity up to 30 m depth AVS_{30} (m/s), and top depth of the layer whose S-wave velocity is 1,400 m/s Z_{1400} (m). We assumed a point source for simplicity. Figure 3 shows the relationship between these variables. The catalog of moment tensor solutions in NIED F-net[21], [22] was referenced for the moment magnitude and source depth. The epicenter of the JMA unified hypocenter catalog and the centroid depth of the F-net moment tensor solutions were referenced while calculating the hypocentral distance. For AVS_{30} and Z_{1400}, we referred to the site-below underground information from the AVS_{30} map of Japan version 3[24], and a deep subsurface structure mode of Japan V2[25] was referenced for Z_{1400}, both of which are available on the website of the Japan Seismic Hazard Information Station (J-SHIS)[23]. Figure 3 shows that the logarithm of X has a strong positive correlation with the logarithm of D_{MAX95}.
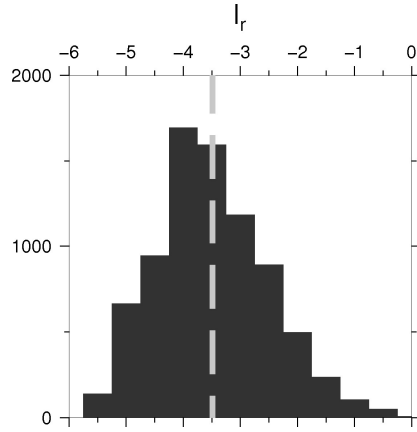
Fig. 2   Histogram of real-time seismic intensity 2 s before the arrival of P-wave; the gray dashed line shows the average value.
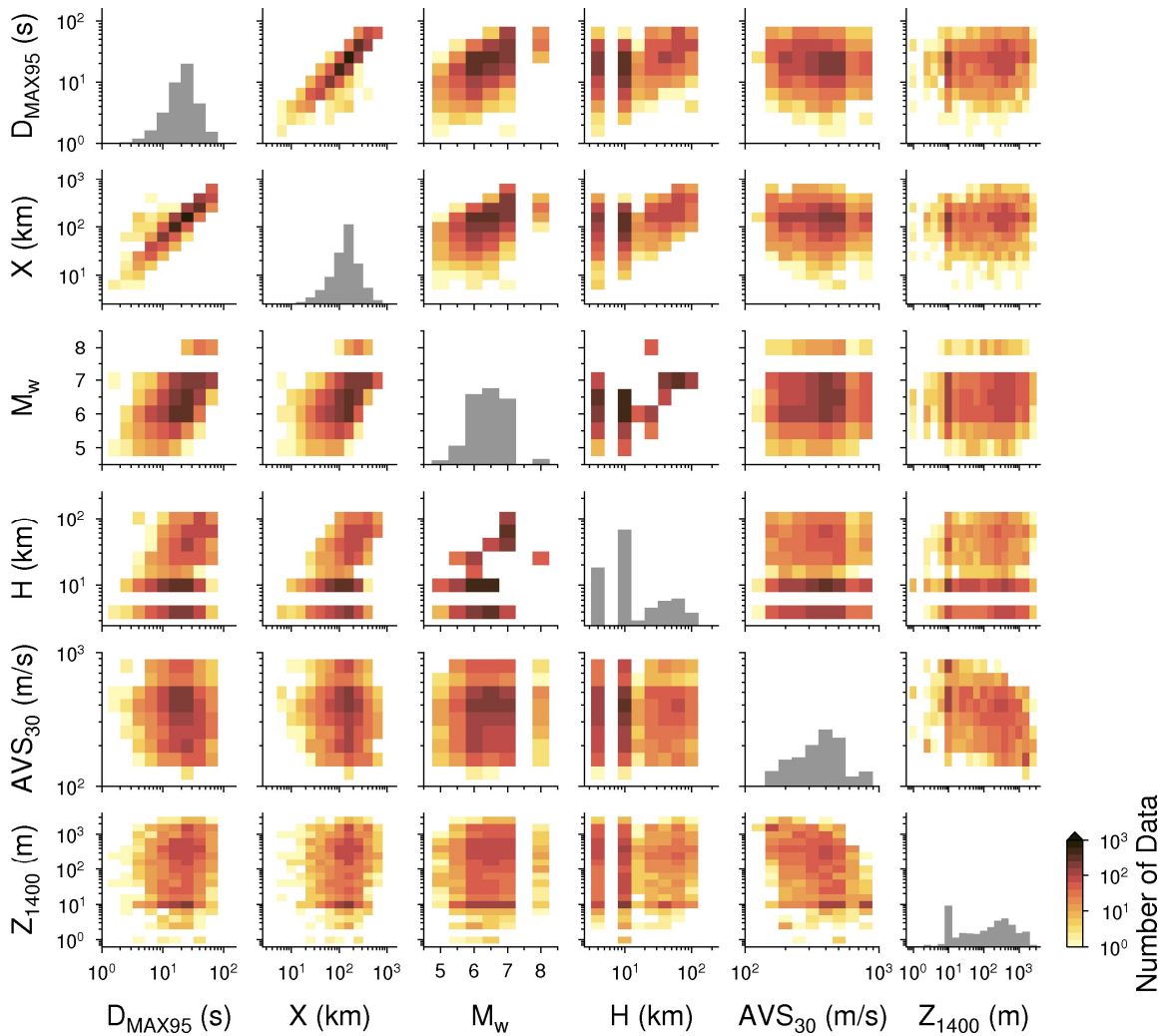

Fig. 3   Relationships between D_{MAX95} (s), hypocentral distance X (km), moment magnitude M_w, source depth H (km), average S-wave velocity up to 30 m depth AVS_{30} (m/s), and top depth of the layer whose S-wave velocity is 1,400 m/s Z_{1400} (m).

A multiple regression equation with five explanatory variables $(X, M_w, H, AVS_{30}, Z_{1400})$ was developed as a prediction equation for D_{MAX95}:

$$\log D_{MAX95} = a \cdot \log X + b \cdot M_w + c \cdot \log H + d \cdot \log AVS_{30} + e \cdot \log Z_{1400} + f \tag{3}$$

In Eq. (3), the base of all logarithms is 10. The partial regression coefficients (a, b, c, d, e, f) in Eq. (3) were estimated by a linear regression analysis of statsmodels[26].

Table 1 shows the estimated partial regression coefficients. The partial regression coefficient of $\log X$, a, is positive, which indicates that a larger hypocentral distance results in a longer D_{MAX95}. This corresponds to the strong positive correlation between the logarithm of X and the logarithm of D_{MAX95} seen in Fig. 3, and is consistent with the trend of the travel-time difference between the P- and S-waves. The partial regression coefficient of M_w, b, is also positive, which corresponds to the fact that a larger earthquake magnitude results in a longer rupture duration and a delayed peak time of the source time function. The partial regression coefficient of $\log H$, c, is negative, which indicates that a deeper earthquake results in a shorter D_{MAX95}. Intraslab earthquakes and deep earthquakes possess a larger stress drop than that of earthquakes of other types and shallow earthquakes[27], [28]. Earthquakes with a large stress drop have a small fault area with respect to their earthquake magnitude, and a small fault area leads to a short rupture duration, which is consistent with our analysis result. Furthermore, compared to deep earthquakes, shallow earthquakes are more likely to induce a predominance of subsequent waves, including surface waves. The partial regression coefficient of AVS_{30}, d, is negative, and the partial regression coefficient of $\log Z_{1400}$, e, is positive. AVS_{30} and Z_{1400} are site proxies for the softness of shallow soft soils and the thickness of sedimentary layer, respectively. The regression analysis results indicate that a softer shallow soil or thicker sedimentary layer amplifies the ground motion intensity as well as the ground motion duration and delays the peak time of earthquake shaking.

The t-values of the estimated partial regression coefficients, which indicate the influence of each explanatory variable on the objective variable, are also shown in Table 1. The effect of hypocentral distance is larger than that of the other explanatory variables. The explanatory variable statistically exerts no effect on the objective variable if the absolute t-value < 2; however, there are no such explanatory variables in this analysis. Table 2 shows the results of the regression analysis for different combinations of explanatory variables. The value of Akaike Information Criterion (AIC)[29] is best when all five explanatory variables are used, as shown in Eq. (3).

Table 1　Estimated partial regression coefficients and their t-values

	a	b	c	d	e	f
Partial regression coefficient	0.7926	0.0616	−0.0745	−0.0746	0.0098	−0.5108
t-value	229.671	32.272	−32.890	−15.184	12.428	−30.859

Table 2 Coefficient of determination and AIC in regression analysis for different combinations of explanatory variables

Combination of explanatory variables	Coefficient of determination	AIC
$(\log X, M_w)$	0.894	$-1.751 * 10^4$
$(\log X, M_w, \log H)$	0.906	$-1.846 * 10^4$
$(\log X, M_w, \log AVS_{30}, \log Z_{1400})$	0.900	$-1.800 * 10^4$
$(\log X, M_w, \log H, \log AVS_{30})$	0.910	$-1.885 * 10^4$
$(\log X, M_w, \log H, \log Z_{1400})$	0.910	$-1.878 * 10^4$
$(\log X, M_w, \log H, \log AVS_{30}, \log Z_{1400})$	0.912	$-1.899 * 10^4$

Figure 4 shows the residual distribution and its relationships with explanatory variables. In this regression analysis, the standard deviation was 0.0725, and the coefficient of determination was 0.912; thus, the data fitting was good. Some overestimation predictions were found, and they corresponded to the case where the real-time seismic intensity reached its maximum during P-wave. As shown in Fig. 1, most records of real-time seismic intensity attained the maximum time after the S-wave arrival; therefore, the prediction equation of D_{MAX95} proposed in this study is valid in most cases. Figure 4 also shows the average and standard deviation of residuals for fixed intervals of the explanatory variables. No significant trend was identified between the explanatory variable and the standard deviation of residuals. The average of residuals was close to zero in most cases; however, a slight underestimation bias was found for hypocentral distance, $X \leq 20$ km, or moment magnitude, $M_w \geq 7.5$. This could be due to the finiteness of fault rupture for large earthquakes, which reduces the validity of the point source assumption; however, the bias was ≤ 0.05 on the log scale, which is not overly strong.

Previous studies on the prediction of ground motion intensity have developed the prediction equation for each earthquake type, such as inland, interplate, and intraslab earthquakes[4]. However, because the bias of earthquake type is strong in our dataset, as shown in Table A1, a prediction equation for D_{MAX95} was not developed for each earthquake type in this study. However, in this study, the source depth was adopted as an explanatory variable in the prediction equation of D_{MAX95}, as shown in Eq. (3). Intraslab earthquakes possess a deeper source depth than other earthquake types. Therefore, the difference between intraslab earthquakes and other earthquake types is indirectly considered through the use of the source depth in the explanatory variables of the prediction equation.
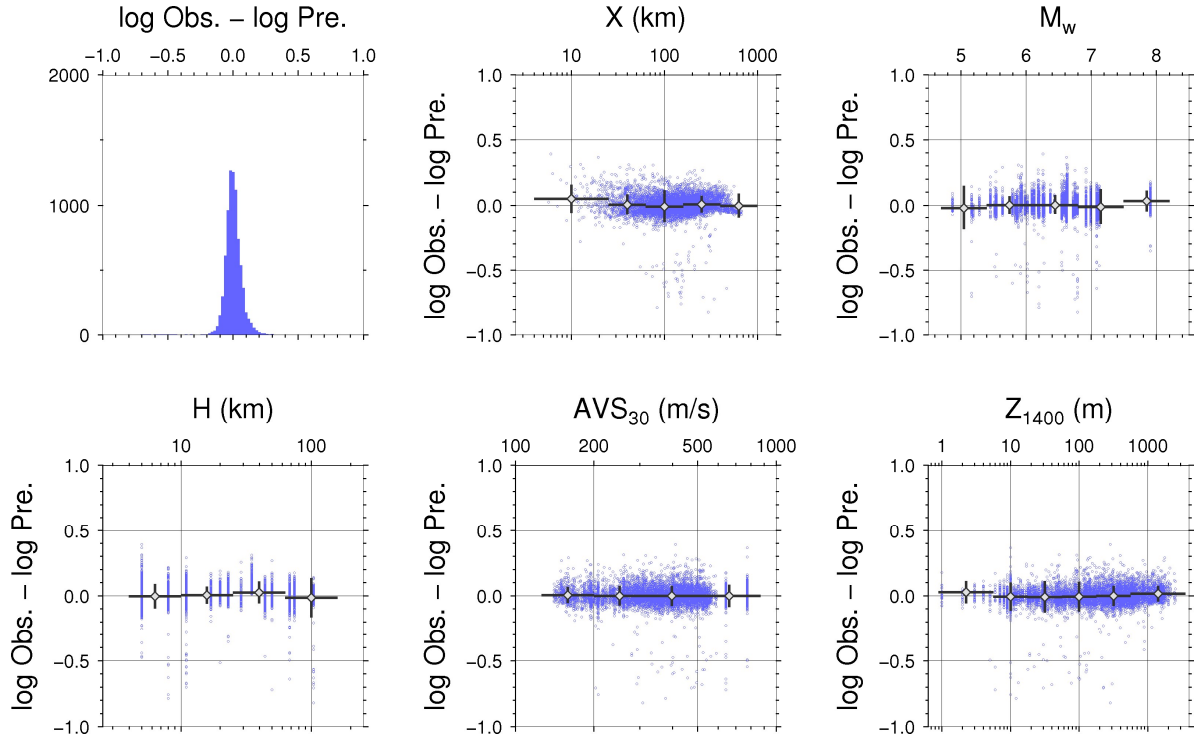
Fig. 4 Residual distribution and its relationships with explanatory variables in the regression analysis of D_{MAX95}. The diamonds represent the average of the residuals within the range of the horizontal line, and the vertical line represents the range of the standard deviation.

3. APPROXIMATION OF RISE-PART TIME SERIES

As shown in Fig. 1, the real-time seismic intensity did not increase linearly and monotonically from the arrival of P-wave, but increased in a convex shape. Therefore, we considered the time series from the arrival of P-wave to the peak of real-time seismic intensity as a single function and devised the following function that approximates it as a logarithmic function:

$$
I_r(t) = \begin{cases} I_r^0 & (t < T_p) \\ 0.95 \times (I_r^{MAX} - I_r^0) \times \frac{\log(t - T_p + \varepsilon) - \log\varepsilon}{\log(D'_{MAX95} + \varepsilon) - \log\varepsilon} + I_r^0 & (T_p \leq t < T'_{MAX}) \\ I_r^{MAX} & (T'_{MAX} \leq t) \end{cases} \tag{4}
$$

$$
T'_{MAX} = T_p - \varepsilon + 10^{\left[\frac{\log(D'_{MAX95} + \varepsilon) - \log\varepsilon}{0.95} + \log\varepsilon\right]} \tag{5}
$$

D'_{MAX95} is the value predicted from Eq. (3). ε is a parameter that sets the degree of convex upward in the logarithmic function, and T'_{MAX} is the time when the real-time seismic intensity is theoretically maximized, which is determined by D'_{MAX95} and ε. The base of all logarithms is 10. Figure 5 schematically shows the prediction time-series of the proposed approximation. I_r takes a value of I_r^0 (−3.5) until the arrival of P-wave (T_p), increases according to the logarithmic function after T_p, and the maximum value, I_r^{MAX}, was attained at T'_{MAX}.

The real-time seismic intensity dataset outlined in Section 2 was used to search for the value of ε that best matched the observations. The root mean square (RMS) between the observed time-series from T_p to T'_{MAX95} and the predicted time-series based on Eqs. (4) and (5) was calculated for each record for various ε values, and the overall average and variation were obtained (Fig. 6). The observed values were used for I_r^{MAX}. The average RMS was smallest at ε = 0.2; therefore, this value was adopted.
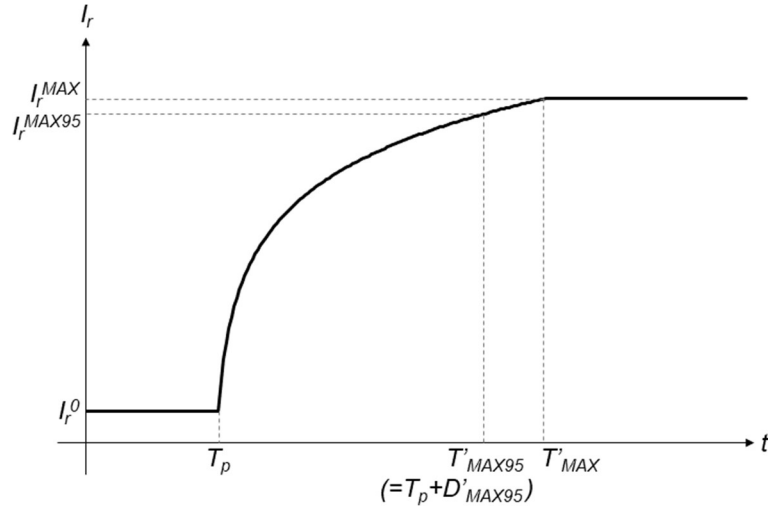

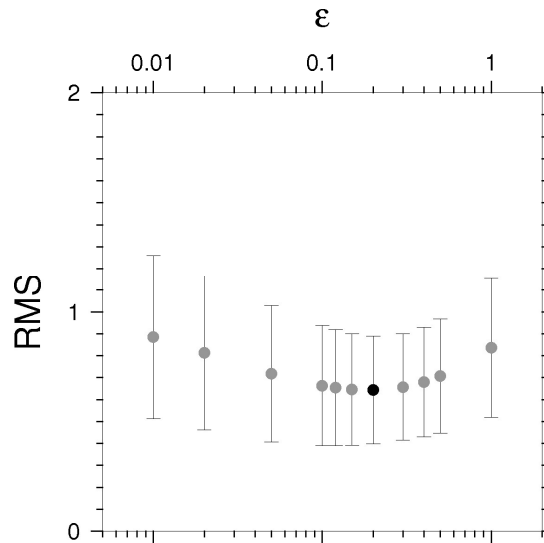Fig. 5　Schematic diagram of the prediction time-series of the proposed approximation

Fig. 6　Relationship between ε and RMS. ε = 0.2 has the smallest average RMS value and is displayed in black.

Figure 7 shows the results of reproducing the observation records in Fig. 1 using the prediction equation of D_{MAX95} in Section 2 and the aforementioned approximate function. D_{MAX95} was calculated based on Eq. (3) from the hypocenter and site information in each record, after which the predicted time-series was obtained according to Eqs. (4) and (5). The observed values were used for I_r^{MAX}. The proposed method could reproduce the time-series shape in most of the observation records within the range of ±1. Figure 8 shows the heat map of the difference between the observed and predicted time-series for all records. The difference between the observed and predicted time-series was within ±1 for most records. The time until the real-time seismic intensity attains the maximum value, as

well as the overall time-series shape, can be roughly reproduced by the proposed method. The prediction of the proposed method could not completely reproduce the observed time-series and is limited by the approximation of the complex time-series of real-time seismic intensity composed of various seismic waves through a single logarithmic function. Further research is required to develop a more sophisticated model that considers the various types of seismic waves.

(a) Event #12 (M_w 6.6), NIG022, X 28.6 km, D_{MAX95} 7.0 s, I_r^{MAX} 5.1

(b) Event #12 (M_w 6.6), GNM009, X 105.8 km, D_{MAX95} 16.9 s, I_r^{MAX} 3.8

(c) Event #14 (M_w 5.8), NIG022, X 34.5 km, D_{MAX95} 5.9 s, I_r^{MAX} 4.2
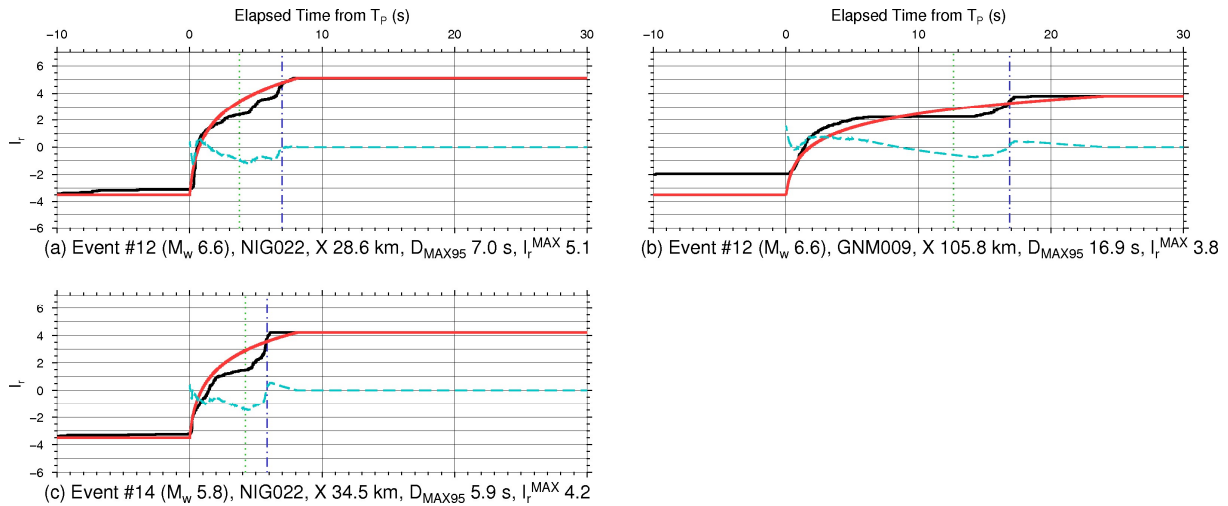
Fig. 7　Prediction examples of real-time seismic intensity for the observations in Fig. 1. The predicted time-series is displayed as a red line, and the difference between the observed and predicted time-series is displayed as a dashed cyan line.
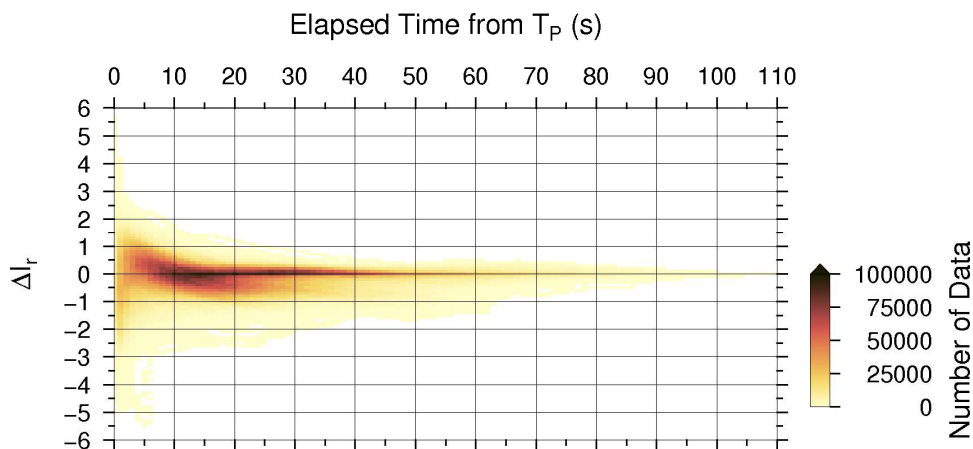

Fig. 8　Heat map of the difference between the observed and predicted time-series for all records

4. VERTIFICATION WITH ACTUAL RECORDS

We applied the proposed approach to the records of earthquakes that were not used in Sections 2 and 3: the 2016 Kumamoto earthquake and the 2011 Tohoku earthquake, to verify its prediction performance. The observed values were used for I_r^{MAX}.

　　The 2016 Kumamoto earthquake was a crustal earthquake that occurred at 1:25 on April 16, 2016 [JST] (M_w 7.1, H 11 km). Figure 9 shows a comparison of the observations and predictions of D_{MAX95} for this earthquake. The absolute value of the residual was less than 0.2 in most records, and

therefore, D_{MAX95} was reproduced to the same extent as in the regression analysis in Section 2. There were some overestimations, and these corresponded to cases where the real-time seismic intensity reached the maximum during P-wave. Figure 10 shows the prediction examples of the real-time seismic intensity for the 2016 Kumamoto earthquake. The predicted values reproduced the observed values within a range of ±1 at KMMH16 (Fig. 10(a)), which is located near the hypocenter, and TTRH03 (Fig. 10(c)), which is located far away from the hypocenter. In OITH11 (Fig. 10(b)), the predicted time-series reached a maximum approximately 5 s earlier than the observations. This underestimation of D_{MAX95} can be found at several observation stations in the Oita Prefecture, including OITH11 (Fig. 9). During the shaking of the 2016 Kumamoto earthquake, an induced earthquake (purple cross in Fig. 9) occurred in the Oita Prefecture[30]. At several observation stations, including OITH11, the ground motions caused by this induced earthquake were stronger than that caused by the 2016 Kumamoto earthquake[30]. The real-time seismic intensity time-series at these stations were also strongly impacted by the induced earthquake, which resulted in the underestimation of D_{MAX95}.
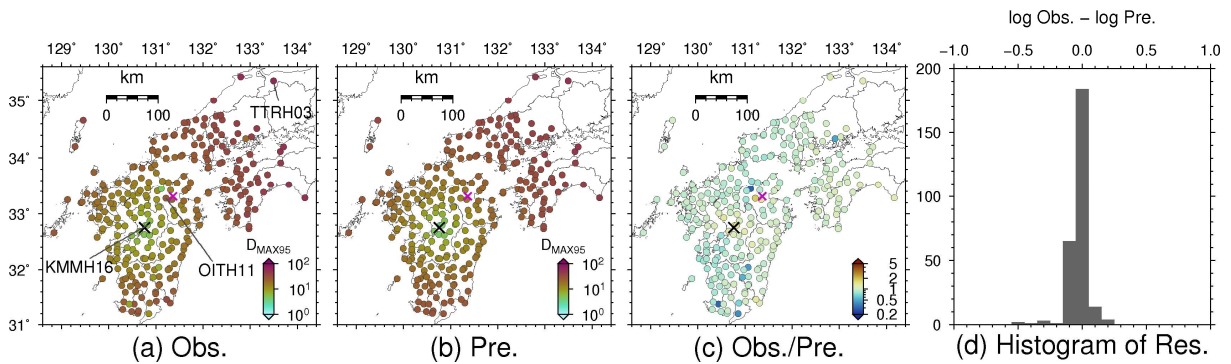

Fig. 9 D_{MAX95} distribution of the 2016 Kumamoto earthquake: (a) observations, (b) predictions, (c) residuals between the observations and predictions, and (d) histogram of the residuals. The black cross indicates the epicenter of this earthquake, and the purple cross indicates the epicenter of the induced earthquake[30].
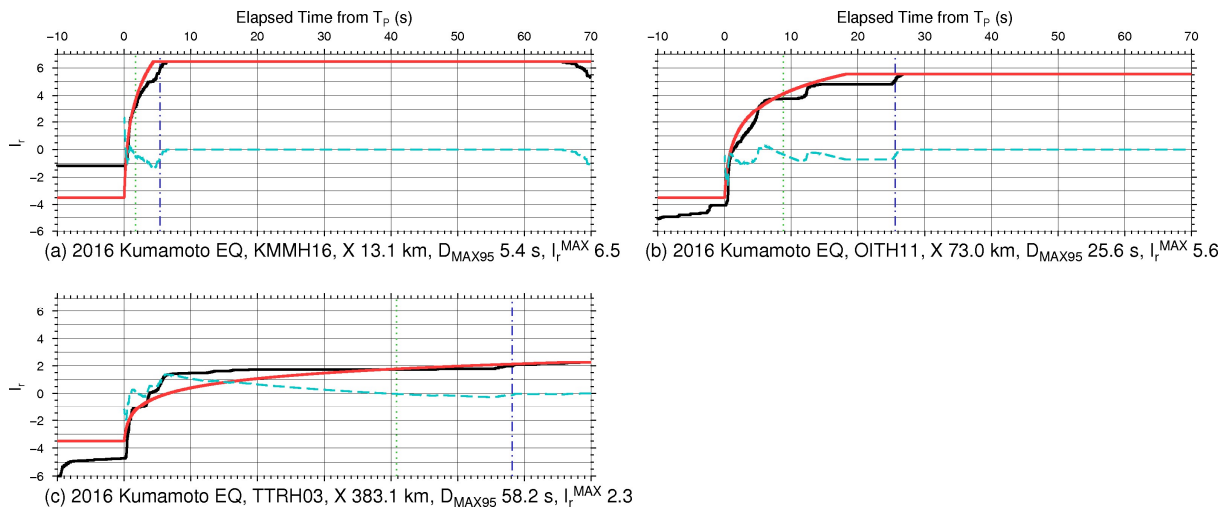

Fig. 10 Observed records of real-time seismic intensity for the 2016 Kumamoto earthquake and its predictions.

The 2011 Tohoku earthquake, which was an enormous plate-boundary earthquake, occurred at 14:46 on March 11, 2011; its magnitude (M_{JMA} 9.0, F-net M_w 8.7) greatly exceeded the range of earthquake magnitudes in the dataset used in our regression analysis of D_{MAX95}. Furthermore, this earthquake had a complex fault rupture with a wide source area[31), 32)]; the application of the proposed method assuming a point source is difficult. Because it is important to investigate the prediction performance in the case of such extrapolations, we intentionally sought to verify the proposed method through the records of the 2011 Tohoku earthquake. The F-net moment tensor solution (M_w 8.7, H 20 km) was used as the source information for this earthquake. Figure 11 shows a comparison of the observations and predictions of D_{MAX95}. In the areas north of 38°N, such as the Miyagi and Iwate Prefectures, the observation of D_{MAX95} was reproduced to the same extent as in the regression analysis in Section 2 and as in the 2016 Kumamoto earthquake. However, D_{MAX95} was systematically underestimated in the areas south of 38°N, such as the Fukushima and Ibaraki Prefectures. Figure 12 shows the prediction examples of the real-time seismic intensity for this earthquake. The predicted peak time of real-time seismic intensity was shifted to approximately 50 s before the observed value at FKSH14 (Fig. 12(c)) in the Fukushima Prefecture. Previous studies on the rupture process of the 2011 Tohoku earthquake revealed that the fault rupture mainly occurred off the Miyagi Prefecture for approximately 100 s from the rupture initiation, after which the fault rupture progressed to the off-regions of the Fukushima and Ibaraki Prefectures[31), 32)]. The complexity of this fault rupture contributes to the extension of the shaking duration in the areas south of the Fukushima Prefecture, which caused the peak delay of real-time seismic intensity. The predicted time-series was larger than the observations not only at FKSH14 but also at IWTH21 (Fig. 12(a)) in the Iwate Prefecture and at MYG011 (Fig. 12(b)) in the Miyagi Prefecture. This difference is expected to be due to the complexity of the fault rupture process and seismic wave radiation process of this earthquake, in which strong motions were generated multiple times at multiple locations with time lags.
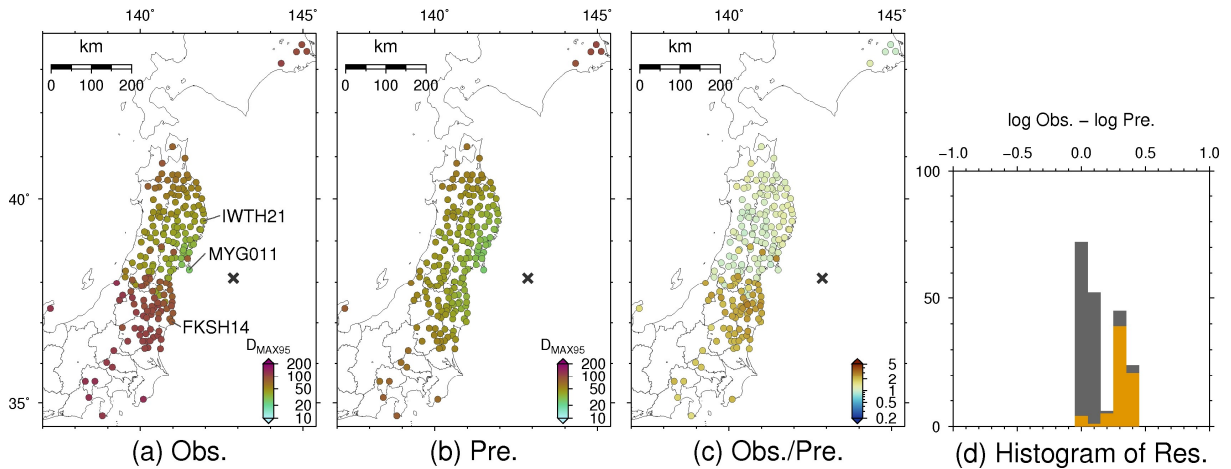

Fig. 11 D_{MAX95} distribution of the 2011 Tohoku earthquake: (a) observations, (b) predictions, (c) residuals between the observations and predictions, and (d) histogram of the residuals. The cross indicates the epicenter of this earthquake. The orange bar in the histogram indicates the residual at the stations south of 38°N.
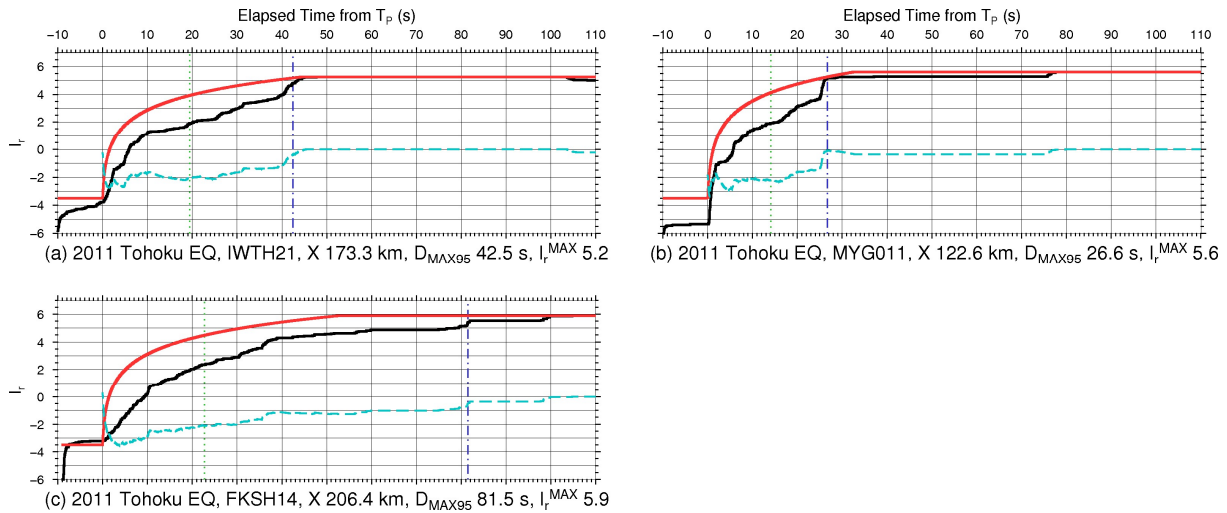
Fig. 12 Observed records of real-time seismic intensity observation records for the 2011 Tohoku earthquake and its predictions

5. CONCLUSIONS

To simply predict and reproduce the rise part of real-time seismic intensity, we proposed a prediction method that combined the following approaches:

1. The development of a prediction equation that relates the rise time from the P-wave arrival until 95% of the maximum real-time seismic intensity D_{MAX95} with the hypocentral distance, moment magnitude, source depth, average S-wave velocity up to 30 m depth, and top depth to the layer whose S-wave velocity is 1,400 m/s based on the regression analysis of the ground motion records of 41 earthquakes.

2. The proposal of a function that approximates the time-series of real-time seismic intensity from the P-wave arrival to its peak based on a logarithmic function.

The application of this prediction approach to actual records demonstrated a good prediction performance, although we also found that the prediction performance was limited when induced earthquakes or massive earthquakes with a fault rupture process occurred.

Combining the prediction method proposed in this study with the existing ground motion prediction equation that predicts the seismic intensity value enables the simple prediction of real-time seismic intensity time-series for any earthquake at any location. The results of this study contribute to the provision of more realistic information on the time-series of ground motions, which can be used in the pre-training of earthquake disasters based on earthquake scenarios. Additionally, our results can contribute to the upgrading of earthquake early warnings (EEW). Although EEW to date has predicted only the maximum value of seismic intensity, this study can facilitate new information on the time-series of shaking (e.g., lead time until the peak shaking).

ACKNOWLEDGMENT

APPENDIX

Table A1 List of earthquakes used for analysis in this study

No.	Date and time of occurrence	M_w	Depth (km)	Earthquake type*	Number of records
1	1997-05-13 14:38	6.0	11	I	59
2	1998-09-03 16:58	5.9	5	I	22
3	2000-07-01 16:01	6.2	5	I	12
4	2000-07-30 21:25	6.4	11	I	14
5	2000-10-06 13:30	6.6	11	I	264
6	2001-03-24 15:27	6.8	50	III	315
7	2003-05-26 18:24	7.0	74	III	379
8	2003-07-26 00:13	5.5	5	I	95
9	2003-07-26 07:13	6.1	5	I	184
10	2003-07-26 16:56	5.3	5	I	47
11	2003-09-26 04:50	7.9	23	II	181
12	2004-10-23 17:56	6.6	5	I	312
13	2004-10-23 18:34	6.3	11	I	264
14	2004-10-27 10:40	5.8	11	I	181
15	2005-03-20 10:53	6.6	11	I	224
16	2005-08-16 11:46	7.1	44	II	286
17	2007-03-25 09:41	6.7	8	I	224
18	2007-07-16 10:13	6.6	8	I	311
19	2007-07-16 15:37	5.6	11	I	99
20	2008-06-14 08:43	6.9	5	I	273
21	2008-07-24 00:26	6.8	104	III	429
22	2009-08-11 05:07	6.2	20	III	318
23	2011-03-12 03:59	6.2	5	I	198
24	2011-03-15 22:31	5.9	8	I	235
25	2011-04-07 23:32	7.1	68	III	515
26	2011-04-11 17:16	6.6	5	I	346
27	2011-04-12 14:07	5.9	8	I	208
28	2013-04-13 05:33	5.8	11	I	201
29	2014-11-22 22:08	6.3	5	I	163
30	2016-04-14 21:26	6.1	17	I	169
31	2016-04-15 00:03	6.0	8	I	131
32	2016-04-16 03:55	5.5	5	I	66
33	2016-04-16 09:48	5.2	11	I	69
34	2016-06-16 14:21	5.2	5	I	23
35	2016-10-21 14:07	6.2	8	I	236
36	2016-12-28 21:38	5.9	5	I	187
37	2018-06-18 07:58	5.5	11	I	216

*Classification of earthquake type—I: crustal earthquake, II: interplate earthquake, III: intraslab earthquake

Table A1 List of earthquakes used for analysis in this study (continued)

No.	Date and time of occurrence	M_w	Depth (km)	Earthquake type*	Number of records
38	2018-09-06 03:07	6.6	35	I	214
39	2019-01-03 18:10	4.9	11	I	51
40	2019-02-21 21:22	5.5	29	I	94
41	2019-06-18 22:22	6.4	11	I	207

*Classification of earthquake type—I: crustal earthquake, II: interplate earthquake, III: intraslab earthquake

REFERENCES

1)   Japan Meteorological Agency: *About Seismic Intensity*, Gyosei, 238 pp., 1996 (in Japanese).

2)   Kunugi, T., Aoi, S., Nakamura, H., Fujiwara, H. and Morikawa, N.: A Real-Time Processing of Seismic Intensity, *Zisin (Journal of the Seismological Society of Japan. 2nd ser.)*, Vol. 60, No. 4, pp. 243–252, 2008 (in Japanese). https://doi.org/10.4294/zisin.60.243

3)   Matsusaki, S., Hisada, Y. and Fukushima, Y.: Attenuation Relation of JMA Seismic Intensity Applicable to Near Source Region, *Journal of Structural and Construction Engineering (Transactions of AIJ)*, Vol. 71, No. 604, pp. 201–208, 2006 (in Japanese). https://doi.org/10.3130/aijs.71.201

4)   Morikawa, N. and Fujiwara, H.: A New Ground Motion Prediction Equation for Japan Applicable up to M9 Mega-Earthquake, *Journal of Disaster Research*, Vol. 8, No. 5, pp. 878–888, 2013. https://doi.org/10.20965/jdr.2013.p0878

5)   Nojima, N.: Conditional Prediction Equations for Duration of Specified Intensity Levels under Given Predicted or Observed JMA Seismic Intensity, *Journal of Japan Association for Earthquake Engineering*, Vol. 14, No. 5, pp. 5_50–5_67, 2014 (in Japanese). https://doi.org/10.5610/jaee.14.5_50

6)   Nojima, N.: Proposal of a Consistent Scheme for Empirical Prediction of JMA Seismic Intensity and Its Duration, *Journal of Japan Association for Earthquake Engineering*, Vol. 15, No. 2, pp. 2_59–2_76, 2015 (in Japanese). https://doi.org/10.5610/jaee.15.2_59

7)   Nojima, N. and Kuse, M.: Application and Validation of the Consistent Scheme for Prediction of JMA Seismic Intensity and its Duration, *Journal of Japan Society of Civil Engineers, Ser. A1 (Structural Engineering & Earthquake Engineering (SE/EE))*, Vol. 72, No. 4, pp. I_44–I_54, 2016 (in Japanese). https://doi.org/10.2208/jscejseee.72.I_44

8)   Bommer, J. J., Stafford, P. J. and Alarcon, J. E.: Empirical Equations for the Prediction of the Significant, Bracketed, and Uniform Duration of Earthquake Ground Motion, *Bulletin of the Seismological Society of America*, Vol. 99, No. 6, pp. 3217–3233, 2009. https://doi.org/10.1785/0120080298

9)   Kempton, J. J. and Stewart, J. P.: Prediction Equations for Significant Duration of Earthquake Ground Motions Considering Site and Near-Source Effects, *Earthquake Spectra*, Vol. 22, No. 4, pp. 985–1013, 2006. https://doi.org/10.1193/1.2358175

10) Bora, S. S., Cotton, F. and Scherbaum, F.: NGA-West2 Empirical Fourier and Duration Models to Generate Adjustable Response Spectra, *Earthquake Spectra*, Vol. 35, No. 1 pp. 61–93, 2019. https://doi.org/10.1193/110317EQS228M

11) Arias, A.: A Measure of Earthquake Intensity, in *Seismic Design for Nuclear Power Plants*, R. J. Hansen (Editor), MIT Press, Cambridge, Massachusetts, pp. 438–483, 1970.

12) Afshari, K. and Stewart, J. P.: Physically Parameterized Prediction Equations for Significant Duration in Active Crustal Regions, *Earthquake Spectra*, Vol. 32, No. 4, pp. 2057–2081, 2016. https://doi.org/10.1193/063015EQS106M

13) Du, W. and Wang, G.: Prediction Equations for Ground-Motion Significant Durations Using the NGA-West2

Database, *Bulletin of the Seismological Society of America*, Vol. 107, No. 1, pp. 319–333, 2016. https://doi.org/10.1785/0120150352

14) Bahrampouri, M., Rodriguez-Marek, A. and Green, R. A.: Ground Motion Prediction Equations for Significant Duration Using the KiK-net Database, *Earthquake Spectra*, Vol. 37, No. 2, pp. 903–920, 2021. https://doi.org/10.1177/8755293020970971

15) National Research Institute for Earth Science and Disaster Resilience: Instrumental Seismic Intensity Approximation Device, Instrumental Seismic Intensity Approximation System Using the Device, and Method for Approximating Instrumental Seismic Intensity, JP4229337, 2008-12-12.

16) National Research Institute for Earth Science and Disaster Resilience: Instrumental Seismic Intensity Approximation Device and Instrumental Seismic Intensity Approximation System Using the Device, JP5946067, 2016-6-10.

17) Aoi, S., Kunugi, T., Nakamura, H. and Fujiwara, H.: Deployment of New Strong Motion Seismographs of K-NET and KiK-net, *Earthquake Data in Engineering Seismology, Geotechnical, Geological, and Earthquake Engineering*, Springer, Vol. 14, pp. 167–186, 2011. https://doi.org/10.1007/978-94-007-0152-6_12

18) National Research Institute for Earth Science and Disaster Resilience: NIED K-NET, KiK-net, 2019. https://doi.org/10.17598/nied.0004

19) Japan Meteorological Agency: Seismic Intensity Database Search, 2021. https://www.data.jma.go.jp/svd/eqdb/data/shindo/index.html (last accessed on September 1, 2022)

20) Ueno, H., Hatakeyama, S., Aketagawa, T., Funasaki, J. and Hamada, N.: Improvement of Hypocenter Determination Procedures in the Japan Meteorological Agency, *Quarterly Journal of Seismology*, Vol. 65, pp. 123–134, 2002 (in Japanese).

21) Fukuyama, E., Ishida, M., Dreger, D. S. and Kawai, H.: Automated Seismic Moment Tensor Determination by Using On-Line Broadband Seismic Waveforms, *Zisin (Journal of the Seismological Society of Japan. 2nd ser.)*, Vol. 51, No. 1, pp. 149–156, 1998 (in Japanese). https://doi.org/10.4294/zisin1948.51.1_149

22) National Research Institute for Earth Science and Disaster Resilience: NIED F-net, 2019. https://doi.org/10.17598/nied.0005

23) National Research Institute for Earth Science and Disaster Resilience: J-SHIS Japan Seismic Hazard Information Station, 2019. https://doi.org/10.17598/nied.0010

24) Matsuoka, M. and Wakamatsu, K.: Amplification Capability Map Based on the 7.5-Arc-Second Japan Engineering Geomorphologic Classification Map, National Institute of Advanced Industrial Science and Technology, Intellectual Property Management No. H20PRO-936, 2008.

25) Fujiwara, H., Kawai, S., Aoi, S., Morikawa, N., Senna, S., Azuma, H., Ooi, M, Hao, K. X., Hasegawa, N, Maeda, T., Iwaki, A., Wakamatsu, K., Imoto, M., Okumura, T., Matsuyama, H. and Narita, A.: Some Improvements of Seismic Hazard Assessment based on the 2011 Tohoku Earthquake, *Technical Note of the National Research Institute for Earth Science and Disaster Resilience*, Vol. 379, pp. 197–200, 2012 (in Japanese).

26) Seabold, S. and Perktold, J.: Statsmodels: Econometric and Statistical Modeling with Python, *Proceedings of the 9th Python in Science Conference*, pp. 92–96, 2010. https://doi.org/ 10.25080/Majora-92bf1922-011

27) Kasatani, N. and Kakehi, Y.: Source Effects of the Intraslab and Interplate Earthquakes off Miyagi Prefecture in Northeastern Japan Based on Spectral Inversion, *Zisin (Journal of the Seismological Society of Japan. 2nd ser.)*, Vol. 67, No. 2, pp. 57–79, 2014 (in Japanese). https://doi.org/10.4294/zisin.67.57

28) Satoh, T.: Short-period Spectral Level of Intraplate and Interplate Earthquakes Occurring off Miyagi Prefecture, *Journal of Japan Association for Earthquake Engineering*, Vol. 4, No. 1, pp. 1–4, 2004 (in Japanese). https://doi.org/10.5610/jaee.4.1

29) Akaike, H.: A New Look at the Statistical Model Identification, *IEEE Transactions on Automatic Control*, AC-19, No. 6, pp. 716–723, 1974.

30) Suzuki, W., Aoi, S., Kunugi, T., Kubo, H., Morikawa, N., Nakamura, H., Kimura, T. and Fujiwara, H.:

Strong Motions Observed by K-NET and KiK-net during the 2016 Kumamoto Earthquake Sequence, *Earth, Planets and Space*, Vol. 69, 19, 2017. https://doi.org/10.1186/s40623-017-0604-8

31) Asano, K. and Iwata, T.: Source Model for Strong Ground Motion Generation in the Frequency Range 0.1–10 Hz during the 2011 Tohoku Earthquake, *Earth, Planets and Space*, Vol. 64, No. 6, 2012. https://doi.org/10.5047/eps.2012.05.003

32) Suzuki, W., Aoi, S., Sekiguchi, H. and Kunugi, T.: Rupture Process of the 2011 Tohoku-Oki Mega-Thrust Earthquake (M9.0) Inverted from Strong-Motion Data, *Geophysical Research Letters*, Vol. 38, L00G16, 2011. https://doi.org/10.1029/2011GL049136

33) Wessel, P. and Smith, W. H. F.: New Improved Version of the Generic Mapping Tools Released, *Eos Transactions*, American Geophysical Union, Vol. 79, pp. 579, 1998.